Comparison of Low and High-Fidelity Models in Structural Optimization of Strut-Braced Wings

Irene Pareja González
irenepareja@tecnico.ulisboa.pt

Instituto Superior Técnico, Universidade de Lisboa, Portugal

September 2021

Abstract

The aim of this thesis is to study the applicability of a Low-Fidelity (LF) structural model for analyzing a given Strut-Braced Wing (SBW) configuration within an optimization environment. To accomplish this goal, the behavior of the structure when subjected to two aerodynamic loads, cruise and pull-up, is firstly compared with a High-Fidelity (HF) model, and then a match between both models is sought. Two optimization problems, one unconstrained and another constrained, set to match the deformed shape of the LF model in the HF one for cruise conditions by changing the thickness distribution, are defined and solved. An additional constrained problem that allows changing the twist distribution is defined as well. Mass and stress for pull-up maneuver conditions are set as constraints for the two constrained problems. A feasible solution in terms of stress is only found when the twist distribution is set as a design variable. However, when analyzing the deformation, the optimized HF model is observed to have differences relative to the LF model higher than 10%. Even though the LF model is computationally advantageous, it underestimated both stress and deformation when compared to the HF model. Therefore, the LF model should only be used to provide general trends at a preliminary design phase of a SBW structure. For a more advanced design stage the HF model should be employed.

Keywords: High-Fidelity Structural Model; Strut-Braced Wing; Structural Design and Optimization; Finite Element Model.

1. Introduction

This thesis aims at studying a Strut-Braced Wing (SBW) which is one of the configurations being proposed for the next generation of commercial aircraft. In order to design it the most efficiently way possible, computational tools that integrates the main aircraft disciplines in one problem such as MDO are desired. However, in a typical aircraft the high dimensionality of the problem might turns these computational tools very costly timewise. Thus, multi-fidelity approaches within MDO are being developed and applied to aircraft design problems.

An overview of the SBW and MDO are given below. In Section 2 the case study, computational tools used and case study results are presented. Section 3 shows the High and LF results comparison. Section 4 describes the optimization problems and Section 5 details the solution found for them. Finally, in the Conclusions Section the main findings are summarized.

1.1. Strut-Braced Wing (SBW)

The greatest virtues of the SBW are an improvement in fuel consumption and a smaller engine size, which means that the SBW would cost less to operate, limit pollutant emissions and reduce noise pollution in urban airports. However, the main disadvantage to add a strut is the significant drag penalty [1, 2]. Some SBW research projects that have been investigated are the ALBATROS by ONERA (French Aeronautics and Space Research Center) [3] and the SUGAR (Subsonic Ultra Green Aircraft Research) Volt [4] by Boeing. Lockheed Martin Aeronautical Systems (LMAS) and Virginia Polytechnic Institute and State University also have recently done research projects about how to improve fuel savings in transport aircraft [5] using a SBW configuration. The investigations [5, 4, 3] showed that the SBW configuration, in terms of design, allows to increase significantly the wing aspect ratio, reduce the wing sweep angle and profile thickness. In addition, all of them have conclude that SBW configuration has the potential for fuel burn savings, between 5-10% compared to an equivalent conventional configuration [6].

1.2. Multi-fidelity Multidisciplinary Design Optimization (MDO)

MDO allows to incorporate all the relevant disciplines simultaneously obtaining the most desirable trade-off between them [7]. The complexity of MDO in aircraft analysis and design comes from the fact that aerodynamics, structures and performance are coupled. This problem is solved with numerical optimization[8]. MDO has two methodological approaches, monolithic and distributed architectures. Monolithic architectures solve a single optimization problem, while distributed ones solve optimiza-

tion subproblems for each discipline and a system-level optimization problem. Distributed architectures increase the system flexibility and responsiveness but, there is no distributed architecture that converges as rapidly as a monolithic one [9].

The fidelity of multidisciplinary systems depends on the fidelity of each discipline and the complexity of the optimization process. The multi-fidelity calculation method combines low and High-Fidelity (HF) discipline codes [10]. The purpose is to provide a way to minimize the usage of high-fidelity models to reduce overall computational cost [11] and accelerate convergence of the design problem [12]. The conceptual design phase begins with Low-Fidelity (LF) calculations. Once this phase is completed, the preliminary design can start by recurring to medium-fidelity models [10]. HF models include the compressible Euler/Navier-Stokes equations and structural finite element models [13].

To use HF methods is very challenging from the design optimization perspective [14, 15], thus multi-fidelity strategies, especially with surrogate models, are preferred. In [15], they combine multi-fidelity Gaussian process regression and Bayesian optimization to construct probabilistic surrogate models and explore high-dimensional design spaces in a cost-effective manner. In [16], they performed a shape optimization analysis constructing a hierarchical multi-fidelity response surface efficiently combining a linear panel method with an Euler solver. A multi-fidelity method commonly used is the polynomial fitting method developed in [17, 18], but the error has shown to be large in the polynomial interpolation used to fit the high with LF data. Co-Kriging method [19] can be used to construct a multi-fidelity surrogate model with both LF and HF data. An extended Co-Kriging method with higher accuracy has been recently developed in [20].

Traditional coupled aero-structural design optimization [21, 22, 23] of aircraft based on HF models is computationally expensive and inefficient. To improve the efficiency, the key is to predict aero-structural performance of the aircraft [13]. Some researchers developed effective optimization frameworks based on genetic algorithm and all kinds of surrogate models [24, 25, 26, 27, 28] for aerodynamic/structural design optimization. The most popular aero-structural prediction method is the loosely coupled aeroelastic analysis for its simplicity. Another prediction method, which is rarely found in commercial software packages due its complex implementation but is very efficient, is the tightly coupled method [13]. It has been studied a coupled aero-structural wing shape design by using Reynolds-Averaged Navier–Stokes (RANS) solver for aerodynamics and NASTRAN for structures and aeroelasticity [29], which are HF simulation tools. The study concluded that the Euler/RANS solver was still be too expensive for the real-world design environment.

Typically, coupled MDO based on computational fluid dynamics/computational structure dynamics (CFD/CSD) aims to optimize the jig shape of aircraft [30]. There is a methodology named reverse iteration of structural model (RISM) proposed in [30] whose main advantage is that it quadruples the efficiency compared with loosely coupled aeroelastic analysis, maintaining almost the same fidelity of the loosely coupled aeroelastic analysis [30]. In [13], the computation has been done using graphical processing units (GPGPU) to accelerate the RISM and construct a GPU-accelerated RISM whose efficiency can be raised about 239 times compared with the one of the loosely coupled aeroelastic analysis. Aly, in [31], proposed a decoupled approach of aero-structural design optimization to avoid the repeated aerodynamic/structural analyses during CFD/CSD analysis which does not lead to the true optimal solution due to optimizations are conducted sequentially [30].

2. Case Study

2.1. Definition

The case study for which the thickness and its distribution are optimized has two load cases, cruise and pull-up maneuver. The deformation obtained by the HF model has to match the deformation of the LF one in the cruise load case. Additionally, the structure has to support a pull-up maneuver load case without exceeding a stress value. The characteristics of the aircraft and the conditions at cruise and pull-up maneuver are detailed in Table 1.

Table 1: Case study data

	Aircraft data	
Maximum Take Off Mass (MTOM) $[kg]$	30938.83	
Structural mass $[kg]$	3272	
	Cruise	Pull-up Maneuver
Load factor [-]	1g	2.55g
Angle of attack $[deg]$	2.5	3.4
Altitude $[m]$	10668	7620
Air density $[kg/m^3]$	0.3805	0.5489
Airspeed $[m/s]$	225.367	235.349
Mach number [-]	0.76	0.76

The loads for the cruise and pull-up maneuver are obtained from an Aerodynamic Force distribution and its points of application, obtained using a 3D Panel Method code. Initially, the load data was given by distributed forces files. After checking the simulation time, it was imperative to reduce the load files to accelerate the computations due to the computational cost needed when using the distributed forces files made unfeasible the optimization process. The new condensed load files contain the load information at the beam nodes used in the structural model. A comparison of the results applying the distributed and condensed files was made to check if the results from the condensed load were reliable and accurate.

The Boundary Condition set in the model is the restriction of all the degrees of freedom of the nodes located at the wing root, i.e. $y = 0$ of the global coordinate system. The structure is considered to be made of aluminium 7075,

which properties are: density $2800kg/m^3$, Young modulus $72GPa$, Poisson coefficient 0.33, yield stress $400MPa$, and yield stress with safety factor $266MPa$.

The structure modelled was simplified to a wing box whose skin is aligned with the airfoil shape. The wing box starts at a given percentual chord distance behind the leading edge ($x_{WB,s}$) and ends at a prescribed percentual chord distance after the leading edge ($x_{WB,e}$), as shown in Figure 1. The upper and lower surfaces simulate the skin of the structure and the side surfaces simulate the spars of the structure. The skin and spar areas have different thickness values.

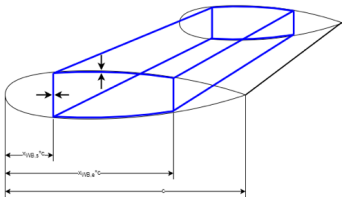

Figure 1: Wing box sketch

2.2. Computational tools

The main computational tool used throughout this project to model and parametrize the geometry is Ansys Parametric Design Language (APDL) [32]. Two type of elements from the Ansys APDL element library were used to conduct the finite element model: SHELL181 and MPC184. The shell elements were used to model the skin and spars of the structure and the MPC elements were used to model the ribs distributed along the structure [33]. The optimization process is carried out in Matlab using the nonlinear programming solvers *fmincon* and *fminunc*.

2.3. Results

As in the optimizations the deformation is computed in cruise flight conditions and the maximum stress value in pull-up maneuver conditions, the vertical displacement and twist compared here are in the former condition and the stress in the latter condition.

2.3.1. High-Fidelity results

Regarding the deformation, the biggest vertical displacement and twist are 0.53m and 1.95 degrees at the main wing tip. The stress plot of the distributed pull-up maneuver load has stress peaks because of the big thickness transitions, ribs or even out of context values. The biggest thickness transition is located at the main wing-strut joint which causes the most abrupt stress change. Each beam node represents a structural rib, which is a structural stiffener. The stress plot shows lower stress lines in the chordwise direction along the whole structure caused by the ribs. Furthermore, the maximum stress computed by the software is located near the wing tip and has a value of 653MPa. This value was ignored since it was deemed out of context due to the fact that it is a very localized stress and do not represent the stress along the wing. If this stress was distributed over a bigger area and there was a physical explanation for the value, it would have been considered. The maximum stress value considered is the one computed at the main wing root (508MPa) which exceeds in 1.91 times the maximum allowable stress limit. Numerical optimization is used to re-distribute the thickness distribution to reduce the maximum stress to be within the stress limits.

2.3.2. Results comparison from condensed and distributed loads

In terms of deformation in the cruise flight condition, the only degree of freedom that presents deviations when using the condensed load file is the twist. The maximum twist difference is found at the tip (0.25 degrees, 12.8%), as shown in Figure 2.3.2.

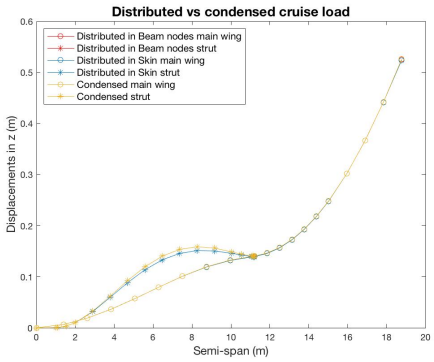

(a) Vertical displacement

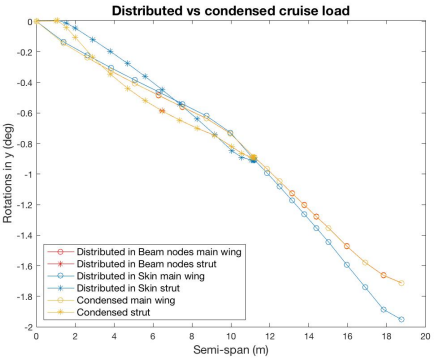

(b) Twist

Figure 2: Results of the distributed and condensed loads

The stress results from applying the pull-up maneuver load revealed that, the distributed load is more conservative than the condensed one. However, the maximum value is almost the same, 508MPa for the distributed load on the skin, and 505MPa for the condensed load, both located at the upper trailing edge of the main wing root. As the maximum stress values do not have large differences, the safety factor used in both optimizations was not modified. Furthermore, they speed up in two orders of magnitude the solving time which made the optimization process feasible.

3. High and Low-Fidelity results comparison

The LF results presented in this section are obtained from an in-house equivalent beam model code [34]. It uses beam elements to represent the wing box showed in Figure 1, while in the HF model shell elements are used to represent the wing structure. This is the main reason for expecting discrepancies in the results. Although both elements can represent the structural model at a preliminary aircraft design level, the beam element model is not able to capture some local phenomena such as buckling of the wing box. As the aim of this thesis is to validate the LF model, the differences between both Fidelity models in terms of deformation and stress are going to be quantified in this section.

3.1. Cruise flight condition

In general, LF underestimates the displacements of the SBW structure in cruise flight conditions. The vertical displacement and twist of the HF and LF models with the baseline thickness distribution is shown in Figure 5, together with the unconstrained optimization solution. The maximum difference between both models in the vertical direction is 2.95cm (32.94%), near the joint region. The twist is underestimated only in the root-joint segment, while it is overestimated in the joint-tip segment. The largest difference in twist is 0.38degrees at one node near the tip.

Regarding the structural stress at the main wing, the LF model is less conservative than the HF model. The root shows big stress differences between both models. The maximum stress in the HF model in cruise flight conditions is 223MPa, near the root, which is more than twice the value estimated by the LF model. However, the LF model overestimates the stress at the main wing-strut joint.

3.2. Pull-up Maneuver flight condition

The differences in vertical displacement and twist reveal that the LF matches well the wing, but not very well the strut. The largest difference in vertical displacement between the HF and LF models is 2.69cm (13.24%) at the middle of the strut. The largest differences in twist increase in the spanwise direction up to 2.13 degrees (30.05%) at the tip.

The main wing stress is underestimated by the LF model. Figure 3 shows at the root big stress differences (87.3%) between both models. At the fairing-strut and main wing-strut joints the LF model underestimates the stress 175MPa and 80MPa, respectively. From this comparison it can be concluded that the baseline thickness distribution is not adequate for the pull-up maneuver case due to the maximum stress estimated by the HF model is 1.91 times higher than the maximum stress allowable.

The LF model is more accurate in cruise flight conditions than in pull-up maneuver conditions. The larger is the load, the bigger the differences will be between both models. Even if the LF model has an advantage in terms of computational cost, the stress results are not well estimated for both flight conditions. The LF model can be used in a preliminary design phase, but not in more advanced phases where a HF model should be used to refine the design.

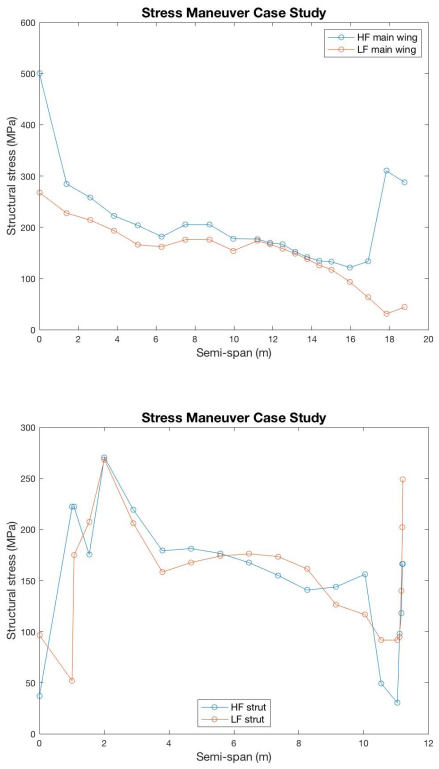

Figure 3: HF and LF models stress results

4. Optimization problem formulation

This project solves three different optimization problems.

4.1. Optimization Problem Statement

The statement of the first optimization problem is to optimize the thickness to obtain the same deformation as the one of the LF model in a cruise flight condition by varying the thickness and its distribution along the main wing and the strut.

The second optimization problem minimizes the structural weight, while trying to obtain the same deformation of the LF model also in a cruise flight condition by varying the thickness and its distribution along the main wing and the strut without exceeding a given value of stress for the pull-up maneuver condition.

Lastly, the statement of the third optimization problem is to match the LF deformation in cruise flight by varying the thickness and its distribution along the main wing and the strut in addition to varying the main wing twist distribution without exceeding a given value of stress and structural mass in the pull-up maneuver.

4.2. Design Variables

The first two optimization problems have the same design variables (x_1 to x_{13}) which are detailed in Table 2. After checking the results of the second problem, it was

decided to add two more kinks to the main wing thickness distribution to give more design freedom, being 25 design variables in total (x_1 to x_{25}). The third optimization problem adds 10 more design variables, which corresponds to the main wing twist distribution, to the 25 defined for the second problem with the two additional kinks (x_1 to x_{35}). All the design variables are detailed in Table 2, as well as their lower and upper bounds.

Table 2: Design variables

Variable	Lower bound	Upper bound	Description
x_1 $[mm]$	1	150	Skin thickness at the root
x_2 $[mm]$	1	34	Skin thickness at the joint inboard
x_3 $[mm]$	1	40	Skin thickness at the joint outboard
x_4 $[mm]$	0.1	30	Skin thickness at the tip
x_5 $[mm]$	1	150	Spar thickness at the root
x_6 $[mm]$	1	34	Spar thickness at the joint inboard
x_7 $[mm]$	1	30	Spar thickness at the joint outboard
x_8 $[mm]$	0.1	30	Spar thickness at the tip
x_9 $[mm]$	10	100	Strut thickness at the joint
x_{10} $[mm]$	1	50	Main strut thickness
x_{11} $[mm]$	10	100	Strut thickness at the fairing
x_{12} [%]	5	25	Kink position at the joint, % of strut
x_{13} [%]	75	95	Kink position at the fairing, % of strut
x_{14} $[mm]$	1	150	Skin thickness at the first kink inboard
x_{15} $[mm]$	1	150	Skin thickness at the first kink outboard
x_{16} $[m]$	0	10	Skin first kink position, span length
x_{17} $[mm]$	1	150	Spar thickness at first kink inboard
x_{18} $[mm]$	1	150	Spar thickness at first kink outboard
x_{19} $[m]$	0.01	10	Spar second kink position, span length
x_{20} $[mm]$	0.1	30	Skin thickness at the second kink inboard
x_{21} $[mm]$	0.1	30	Skin thickness at the second kink outboard
x_{22} $[m]$	10.70	18.77	Skin second kink position, span length
x_{23} $[mm]$	0.1	30	Spar thickness at second kink inboard
x_{24} $[mm]$	0.1	30	Spar thickness at second kink outboard
x_{25} $[m]$	10.70	18.77	Spar second kink position, span length
x_{26} $[deg]$	0	5	Initial twist of the first main wing airfoil
x_{27} $[deg]$	-0.5	5	Initial twist of the second main wing airfoil
x_{28} $[deg]$	-3	5	Initial twist of the third main wing airfoil
x_{29} $[deg]$	-3	5	Initial twist of the fourth main wing airfoil
x_{30} $[deg]$	-3	5	Initial twist of the fifth main wing airfoil
x_{31} $[deg]$	-3	5	Initial twist of the sixth main wing airfoil
x_{32} $[deg]$	-3	5	Initial twist of the seventh main wing airfoil
x_{33} $[deg]$	-3	5	Initial twist of the eighth main wing airfoil
x_{34} $[deg]$	-3	3	Initial twist of the ninth main wing airfoil
x_{35} $[deg]$	-3	3	Initial twist of the tenth main wing airfoil

4.3. Objective function

In the first optimization problem the objective function, which is shown in Equation 1, measures how far or how close is the deformation obtained by HF model with respect to the LF one for the cruise flight condition. To do so, it was used the Mean Square Error (MSE), which measures the average squared difference between the estimated value, i.e. the one from the HF model, and the actual value, i.e. the one from the LF model. The displacement and rotation MSE are multiplied by factors that include the dimensionalization required to sum both. These factors were obtained from an objective function study of the unconstrained optimization and they are also used in Equations 3 and 5. The objective function study finds out which factors minimize the objective function, while requiring a low structural mass without increasing considerably the maximum stress.

$$MSE = \frac{1}{n}\sum_{i=1}^{n}(0.05\cdot(\Delta x_i - \Delta\hat{x_i})^2 + +0.05\cdot(\Delta y_i - \Delta\hat{y_i})^2 + \\ + 0.05\cdot(\Delta z_i - \Delta\hat{z_i})^2) + \frac{1}{n}\sum_{i=1}^{n}(0.25\cdot(\Delta\theta_{x_i} - \Delta\hat{\theta}_{x_i})^2 + \\ + 0.4\cdot(\Delta\theta_{y_i} - \Delta\hat{\theta}_{y_i})^2 + 0.2\cdot(\Delta\theta_{z_i} - \Delta\hat{\theta}_{z_i})^2) \quad (1)$$

The objective of the second optimization problem is to minimize the structural mass which is shown in Equation 2. To do so, the structural mass resulting from the optimization (M) is divided by the one of the LF model (M_0) detailed in Table 1.

The objective of the third optimization problem, is to minimize the differences in deformation between both models. Ideally, this difference should be lower than 10%, which does not happen neither in the unconstrained nor in the constrained optimizations. For practicality reasons, it was used the same function defined as deformation constraint in the constrained optimization, shown in Equation 3.

$$f(x) = \frac{M}{M_0} \quad (2)$$

$$f_1(x) = 0.05\cdot max(|\frac{\Delta x - \Delta x_0}{\Delta x_0}|) + 0.05\cdot max(|\frac{\Delta y - \Delta y_0}{\Delta y_0}|) + \\ + 0.05\cdot max(|\frac{\Delta z - \Delta z_0}{\Delta z_0}|) + 0.25\cdot max(|\frac{\Delta\theta_x - \Delta\theta_{x_0}}{\Delta\theta_{x_0}}|) + \\ + 0.4\cdot max(|\frac{\Delta\theta_y - \Delta\theta_{y_0}}{\Delta\theta_{y_0}}|) + 0.2\cdot max(|\frac{\Delta\theta_z - \Delta\theta_{z_0}}{\Delta\theta_{z_0}}|) - 1 \quad (3)$$

A second objective function, shown in Equation 4, was tried in the new constrained optimization to check if a better solution than the one computed with Equation 3 could be provided. As some of the beam nodes have small values in some of the displacements or rotations, the differences in the second objective function are only computed at the wing tip, since the largest displacements and rotations are found there.

$$f_2(x) = 0.05\cdot(|\frac{x_{tip} - x_{0_{tip}}}{x_{0_{tip}}}|) + 0.05\cdot(|\frac{y_{tip} - y_{0_{tip}}}{y_{0_{tip}}}|) + \\ + 0.05\cdot(|\frac{z_{tip} - z_{0_{tip}}}{z_{0_{tip}}}|) + 0.25\cdot(|\frac{\theta_{x_{tip}} - \theta_{x_{0tip}}}{\theta_{x_{0tip}}}|) + \\ + 0.4\cdot(|\frac{\theta_{y_{tip}} - \theta_{y_{0tip}}}{\theta_{y_{0tip}}}|) + 0.2\cdot(|\frac{\theta_{z_{tip}} - \theta_{z_{0tip}}}{\theta_{z_{0tip}}}|) - 1 \quad (4)$$

4.4. Constraints

The first optimization problem is unconstrained, so the optimizer has absolute freedom in all the parameters to match the objective. On the other hand, the second and third optimization problems are constrained.

The constraints of the second optimization problem are: the deformation (Equation 5), that should be the same as

the one obtained with the LF model within a margin (m); and the stress in the pull-up maneuver (Equation 6), that should not exceed the ultimate strength of the material taking into account the safety factor (1.5).

$$g_1 = 0.05 \cdot max(|\frac{\Delta x - \Delta x_0}{\Delta x_0}|) + 0.05 \cdot max(|\frac{\Delta y - \Delta y_0}{\Delta y_0}|) + \\ + 0.05 \cdot max(|\frac{\Delta z - \Delta z_0}{\Delta z_0}|) + 0.25 \cdot max(|\frac{\Delta \theta_x - \Delta \theta_{x_0}}{\Delta \theta_{x_0}}|) + \\ + 0.4 \cdot max(|\frac{\Delta \theta_y - \Delta \theta_{y_0}}{\Delta \theta_{y_0}}|) + 0.2 \cdot max(|\frac{\Delta \theta_z - \Delta \theta_{z_0}}{\Delta \theta_{z_0}}|) - m \quad (5)$$

$$g_2 = \frac{\sigma - \sigma_{max}}{\sigma_{max}} \quad (6)$$

In the above equation, Δ and Δ_0 are the displacements and rotations of the HF and LF models, respectively. The never exceed stress is $\sigma_{max} = 266$ MPa.

Since the constraint has to be a scalar and not an array with all the MSE values, instead of computing the MSE for the deformation constraint, it was used the maximum relative error for each degree of freedom as shown in Equation 5.

The constraints of the third optimization problem are the stress (Equation 6), as in the second optimization problem, and the structural mass (M), that should not exceed 220% of the LF mass (M_0 + 3600kg), as detailed in Equation 7. This percentage could seem very high, but the Baseline thickness distribution used in the LF model (1928.5kg) does not support the pull-up maneuver load stresses and the results of the second constrained optimization showed that a big increase in mass is necessary to support the pull-up maneuver load.

$$g_2 = \frac{M - M_0}{M_0} - 2.2 \quad (7)$$

Since the solutions of the second optimization problem resulted in stiffer structures than the LF one, it is required to limit the amount of material. The more structural mass, the more rigid it will be.

4.5. Algorithm implemented

Fmincon and *fminunc* have different algorithm options. For the unconstrained optimization it was selected the Quasi-Newton option and for both constrained optimizations it was selected the Interior Point Method since it is a good option to obtain a feasible solution due to this algorithm tries first to reach a feasible solution and then it minimizes the objective function.

5. Optimization results

5.1. Unconstrained optimization

The optimized spar and skin thickness distributions together with the baseline thickness distribution are shown in Figure 4. The optimized one presents thickness values that fit inside the airfoils. Furthermore, the joints are located within the bounds used in the constrained optimization. For these reasons, from a geometrical perspective the solution is feasible.

In Table 3 it is presented the maximum stress which exceeds the maximum value allowable (266MPa). As the maneuver load is much larger than the cruise one, the maximum stress will be much higher for that flight condition, which means that the solution obtained from the unconstrained optimization is not realistic in terms of stress for the Case Study. This table also presents the structural mass together with the vertical displacement and twist for the Baseline and Optimized thickness distributions. These latter magnitudes are the absolute maximum differences found between HF and LF models, as indicated in the table heading. The differences in vertical displacement are lower in the Optimized distribution than in the Baseline one, but the twist difference is slightly higher. In Figure 5 it can be seen that the maximum difference between the HF and LF models occur at the tip, where the Optimized distribution has a larger twist value than the Baseline one. If the whole twist graph is observed, it can be concluded that the Optimized thickness distribution matches better the LF twist than the Baseline one, even if the maximum difference value does not suggest it.

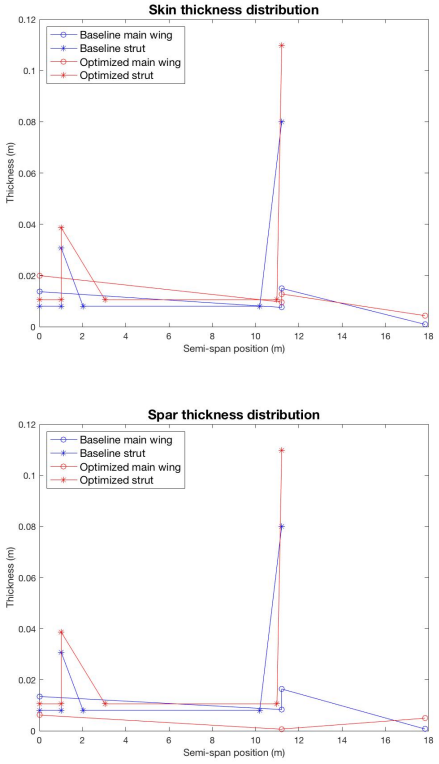

Figure 4: Thickness distribution - unconstrained optimization

Table 3: Unconstrained optimization results

Thickness distribution	Structural weight $[kg]$	Stress max $[MPa]$	$[m]$ max($\|HF - LF\|_z$)	$[°]$ max($\|HF - LF\|_{\theta_y}$)
Baseline	1928.5	225	0.0295	0.3799
Optimized	2295.6	290	0.0089	0.3931
	Structural weight $[kg]$	Stress max $[MPa]$	Vertical disp. at tip $[m]$	Twist at tip $[°]$
Low-Fidelity	1636	110	0.5063	2.3222

In general, the optimized solution has larger skin thickness at the whole structure, larger spar thickness at the strut and fairing but smaller main wing spar thickness than the baseline one, which results in an increase of mass. The reason is that, to be able to match better the deformation, the optimizer is stiffening the structure. However, it is more flexible in twist at the whole structure, but not at the tip where it has the same twist value of the baseline.

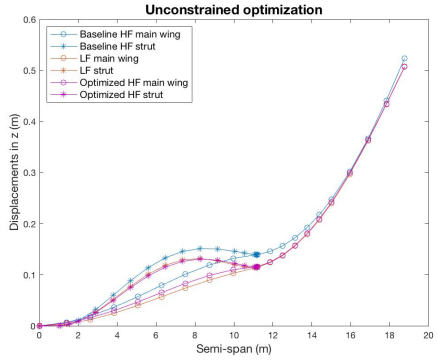

(a) Vertical displacement

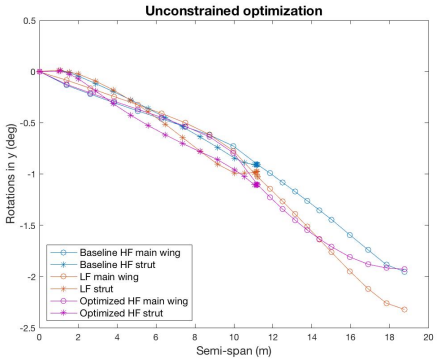

(b) Twist

Figure 5: Results from the optimized thickness distribution

To conclude the unconstrained optimization, the deformation computed with the optimized thickness distribution gets values that match considerably well the LF model deformation, being lower than 10% the maximum difference between the HF and LF models in all the displacements and rotations, except for the twist where the maximum difference of 17% is noticed at the tip. In addition, the maximum stress value computed exceeds the stress limit, being 2.64 times higher than the one from the LF model.

5.2. Constrained optimization

The changes made during the constrained optimization to try to obtain the best result possible within the limitations are detailed next. First of all, the results with the baseline upper and lower boundaries of the design variables were computed. These results revealed that the boundaries were too tight, thus they were increased to provide more freedom to the optimizer, this new set of boundaries is shown in Table 2. Nevertheless, the optimizer could not find a solution in the feasible region. As the deformation continued being larger than the one desired, there were included two additional kinks in the main wing thickness distribution, one in each half of it. The additional kinks were included to allow a higher design freedom in the optimization process and, consequently, try to better match the deformation between HF and LF models. As in the optimizations with the old and new bounds discussed previously, this optimization ended up converging to an infeasible point, since the optimizer was not able to satisfy the constraints.

The first and second constrained optimizations revealed that the two areas that have higher stress values are the main wing root and the joint (inboard part of the wing), thus the optimizer put higher thickness values at these locations. As a localized stress reduction was needed and it was not desired to increase substantially the mass with respect to the baseline mass, it was considered necessary to modify the thickness distributions to give more design freedom to the optimizer to find a solution within the feasible region.

Furthermore, the margin was studied to see the implications of it in terms of mass and stress. The parametric study on the margin concluded that, even if the margin was increased, the optimizer could not get a solution that satisfied the stress constraint by minimizing the mass. As none of the margin values provided a solution that matched the deformation, neither increasing the design variables bounds neither adding two more kinks, a new optimization with different objective and constraint functions was computed to try to reach a feasible solution for this case study.

5.3. Jig shape optimization

In Table 4 are shown the results of the new optimizations performed. The thickness distribution "Opt. 1" and "Opt. 3" were computed with the objective function that compares the HF and LF deformations at all the beam nodes, defined in Equation 3. However, "Opt. 2 - IP" and "Opt. 2 - SQP" were computed with the one that compares only the deformation at the tip, defined in Equation 4. Regarding the constraints, all of them were constrained with Equations 6 and 7, but not "Opt. 3" which allowed to have 2045kg as maximum structural mass. All the thickness distributions were computed with the algorithm interior point except for "Opt. 2 - SQP", which uses the SQP algorithm as its name suggests. The reason to try the same optimization with both algorithms was to see if the SQP could provide a better solution than the interior point one since the optimization with the interior point algorithm converged to a feasible point. However, with the SQP, the optimizer ended up converging to an infeasible point.

Initially, the idea was to constraint the mass up to 2045kg to not increase it a lot in respect to the baseline thickness distribution. After checking the results provided

by "Opt. 3", it was considered necessary to increase the mass allowable to the value shown in Equation 7 to be able to satisfy the stress constraint. "Opt. 3" presented the best twist values, being the differences between the HF and LF lower than 10%. However, the maximum stress is 454MPa, which exceeds in 1.7 times the limit, so it is not a feasible solution even if the goal of the optimization is achieved.

Table 4: Jig shape optimization thickness distribution results

Thickness distribution	Structural mass $[kg]$	Stress max $[MPa]$	Vertical disp. $[m]$ $\max(\lvert HF - LF\rvert_{\theta_x})$	Twist $[°]$ $\max(\lvert HF - LF\rvert_{\theta_y})$
Opt. 1	4803.91	251	0.1933	1.4588
Opt. 2 - IP	3830.51	265	0.0558	1.0953
Opt. 2 - SQP	5290.66	306	0.0953	1.3521
Opt. 3	2096.49	454	0.3605	0.2638

"Opt. 1" and "Opt. 2 - IP" are the only optimizations that converged to a feasible solution, since they satisfy the stress and mass constraints. In Table 4 is shown that the optimization that minimizes the differences at the tip provides a better solution, being the differences in deformation smaller. In Figure 6 are shown "Opt. 1" and "Opt. 2 - IP" thickness distributions. They are shown in the legend as "Deformation at beam nodes" and "Deformation at tip", respectively. "Opt. 2 - IP" in both, skin and spar, has a larger step in the distribution than "Opt. 1", being the kinks located in a more outboard position than the latter. Furthermore, the spar of "Opt. 2 - IP" has larger thickness values in the inboard part of the main wing than "Opt. 1", but not in the skin, where the latter has larger values along the whole main wing and, as a consequence, it has a heavier structure. The fact of adding less material in the skin of the outboard part of the wing makes it more flexible, so it can match better the LF vertical displacement and twist. Regarding the strut thickness, "Opt. 1" presents larger values at the end of the fairing and joint, but lower values at the beginning of the fairing and main strut thickness in both skin and spar. Moreover, it locates both kinks nearer to the root in the inboard direction than "Opt. 2 - IP".

In Figure 6 are shown the vertical displacement and twist of both thickness distributions. It can be seen that the one that compares the deformation at the tip matches better both vertical displacement and twist. Nevertheless, the differences are higher than 10% at the tip, being higher in twist (47%) than in vertical displacement (11%).

In Figure 8 are represented the baseline and "Opt. 2 - IP" twist distributions together with the upper and lower bounds of the twist design variables shown in Table 2. The optimized twist distribution has larger values than the baseline one, being the twist at the last two airfoils at the tip almost coincident.

The new constrained optimization improves the solution with respect to the previous constrained optimization, but the solution provided by the optimizer is just a feasible solution in terms of stress. However, the main goal of the optimization, that is matching the LF model deformation, is not fulfilled due to the differences in deformation between the HF and LF are higher than 10%.

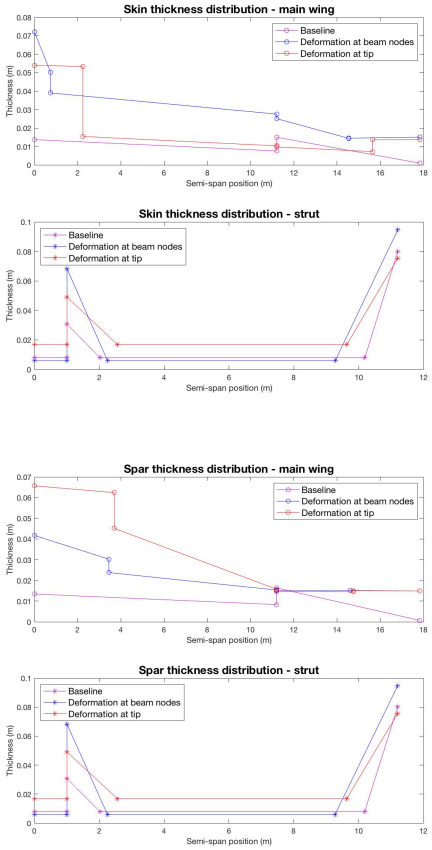

Figure 6: Thickness distributions - jig shape optimization

Margin	Structural weight $[kg]$	Stress max $[MPa]$	Vertical disp. $[m]$ $\max(\lvert HF - LF\rvert_{\theta_x})$	Twist $[°]$ $\max(\lvert HF - LF\rvert_{\theta_y})$
1.5	3315.70	280	0.7251	1.2018
1.5 (+freedom)	3135.54	296	0.0969	1.2194
2.5	3056.03	346	0.0629	1.0333
2.5 (+freedom)	2464.40	414	0.0301	0.9677
3	1876.08	612	0.0592	0.8029
3 (+freedom)	3247.99	289	0.0879	1.1952

Table 5: Parametric study on the Margin - Constrained optimization

6. Conclusions

This work focuses on comparing the structural and shape optimization of HF and LF models for the purpose of validating the LF one. It performs the structural and shape optimization in a HF model to match the deformation resulting from the application of a predetermined cruise load to the LF model for a SBW configuration.

To make the optimization possible, it was imperative to condense the load files provided by the LF model. The results computed using the condensed load files speed up in two orders of magnitude the solving time which made

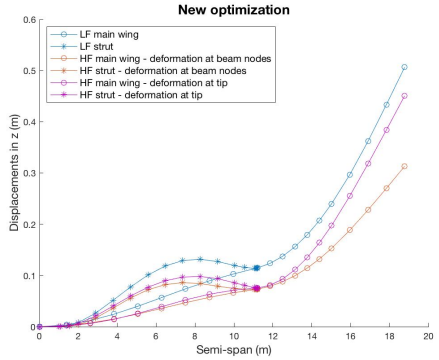

(a) Vertical displacement

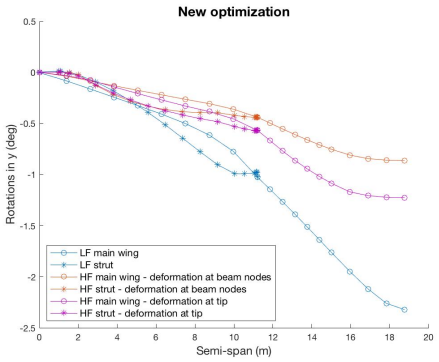

(b) Twist

Figure 7: Results from the jig shape optimization thickness distribution

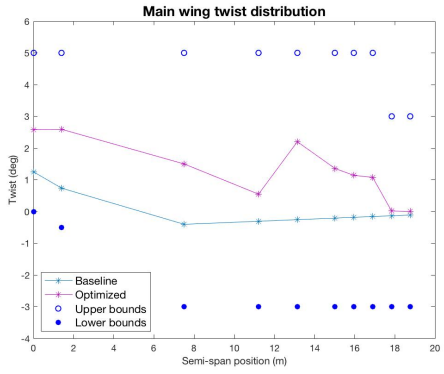

Figure 8: Main wing twist distribution - jig shape optimization

the optimization process feasible. There were found differences only in twist which show that the condensed load twists less the wing than the distributed one. Nevertheless, the differences are still within the admissible values (12.8% in cruise).

There are several results worth summarizing from the comparison between HF and LF models. The main wing and strut stress values were underestimated by the LF model, while the stress at the main wing-strut joint for both flight conditions was overestimated. The HF model maximum stress is 1.91 higher than the one computed by the LF one which made the optimization process difficult. Regarding the deformation, the LF underestimated the value of the displacements. The biggest differences were found in vertical displacement (cruise 32.94%) and twist (maneuver 30.05%) at the strut and wing tip, being the differences larger in maneuver than in cruise since the load is larger. It can be concluded that the LF model has an advantage in terms of computational cost, but for both flight conditions the stress is not well estimated. For these reasons, the LF model can only be used to get a general idea of the deformation of the SBW structure in a preliminary design phase, but not in more advanced phases where a HF model should be used to refine the design.

Regarding the unconstrained optimization, the deformation from the optimized thickness distribution matches the LF one, being all the displacements and rotations within the required tolerances but not the twist, where the outboard part of the main wing exceeds them. The constrained optimization converged to an infeasible point since the optimizer could not find a solution that satisfied the stress constraint and, at the same time, matched the LF deformation. Even broadening the design variables bounds and adding two new kinks to the main wing, the optimizer could not provide a feasible solution. A new optimization with different objective and constraint functions was computed to try to obtain a feasible solution. The new constrained optimization found two feasible solutions in terms of stress, however in terms of deformation both solutions have differences in deformation higher than 10% in comparison with the LF model. Although the new optimization improved the solution with respect to the previous constrained optimization, it was not possible to find a solution that matches the LF deformation within the stress limits.

Further research exploring other objective functions and design variables, such as the dihedral angle, might find a solution that matches the deformation while satisfying the stress constraint. Moreover, other materials, or a combination of them, can be tried to reduce the stress in the high loaded areas, such as the main wing root and the strut joint.

References

[1] F.H. Gern et al. Flexible wing model for structural sizing and multidisciplinary design optimization of strut braced wing. *AIAA*, AIAA 2000-1327, 2000.

[2] B. Wainfan. *Design Process: Braced Wings*, 2020.

[3] G. Carrier et al. Investigation of a strut-braced wing configuration for future commercial transport. *Onera, the French Aerospace Lab, France*, 2012.

[4] M.K. Bradley et al. Subsonic ultra green aircraft research phase ii: volume i– truss braced wing design exploration. *Boeing Research and Technology*, NASA CR-2015-218704, 2015.

[5] F. H. Gern et al. Multidisciplinary design optimization of a transonic commercial transport with a strut-braced wing. *VPI, SU and UF*, 1999.

[6] G. Potter. *Conceptual Design of a Strut-Braced Wing Configuration*, 2017.

[7] J. M. Grasmeyer. Multidisciplinary design optimization of a strut-braced wing aircraft. Master's thesis, VPI and SU, 1998.

[8] J. R. R. A. Martins et al. Multidisciplinary design optimization of aircraft configurations—part 2: High-fidelity aerostructural optimization. *Lecture series, VKIFD*, 2016.

[9] G.N. Vanderplaats. Numerical optimization techniques. computer aided optimal design: Structural and mechanical systems. *Mota Soares*, 1987.

[10] X. Sun et al. Multifidelity multidisciplinary design optimization of integral solid propellant ramjet supersonic cruise vehicles. *National University of Defense Technology, China*, 2019.

[11] T. Robinson et al. Multifi-delity optimization for variable-complexity design. *11th AIAA/ISSMO Multidisciplinary Analysis and Optimization Conference, Virginia*, 2006.

[12] A. March et al. Constrained multifidelity optimization using model calibration. *Department of Aeronautics & Astronautics, Massachusetts Institute of Technology*, 2012.

[13] Y. Zuo, P. Chen, et al. Advanced aerostructural optimization techniques for aircraft design. *NKLADR*, 2015.

[14] N.-V. Nguyen et al. Multidisciplinary unmanned combat air vehicle system design using multi-fidelity model. *Aerospace Science and Technology*, 26, 2013.

[15] L. Bonfiglio et al. A probabilistic framework for md: Application to the hydrostructural optimization of supercavitating hydrofoils. *Int J Numer Methods Eng*, 2018.

[16] S. Choi et al. Multifidelity design optimization of low-boom supersonic jets. *Journal of Aircraft*, 2008.

[17] S. Doyle et al. Developing the aerodynamics module for the integrated multidisciplinary optimization object system. *49th AIAA Aerospace Sciences Meeting*, 2011.

[18] A.-T. Le et al. Building the aerodynamics module for the integrated hypersonic aeromechanics tool. *42nd AIAA Aerospace Sciences Meeting*, 2004.

[19] D.E. Myers. Matrix formulation of co-kriging. *Journal of the International Association for Mathematical Geology*, 14(3), 1982.

[20] M. Xiao et al. Extended co-kriging interpolation method based on multifidelity data. *Applied Mathematics and Computation*, 323, 2018.

[21] L. Cavagna et al. Structural sizing, aeroelastic analysis, and optimization in aircraft conceptual design. *Journal of Aircraft*, 48(6), 2011.

[22] S.S. Ghoman et al. Multifidelity multistrategy and multidisciplinary design optimization environment. *AAIA*, AIAA 2013-4672, 2013.

[23] R.P. Liem et al. Aero- structural design optimization of a 100-passenger regional jet with surrogate-based mission analysis. *13th AIAA Aviation Technology*, AIAA 2013-4372, 2013.

[24] T. Kumano et al. Multi-disciplinary design optimization of wing shape for a small jet aircraft using kriging model. *AAIA*, AIAA 2006-932, 2006.

[25] T. Zill et al. Multi-disciplinary design optimization in a collaborative distributed aircraft design system. *AAIA*, AIAA 2012- 0553, 2012.

[26] S. Rajagopal and R. Ganguli. Multidisciplinary design optimization of a uav wing using kriging based multi-objective genetic algorithm. AIAA 2009-2219, 2009.

[27] M. Nikbay et al. Multi-disciplinary code coupling for analysis and optimization of aeroelastic systems. *Journal Aircraft*, 2009.

[28] Y. Lian et al. Aero-structural optimization of a transonic compressor rotor. *Journal Propul Power*, 2006.

[29] C. Kazuhisa et al. High-fidelity multidisciplinary design optimization of aero-structural wing shape for regional jet. *Springer*, 3410, 2005.

[30] Y.T. Zuo et al. Efficient aero-structural design optimization: Coupling based on reverse iteration of structural model. *Sci China Tech Sci*, 2015.

[31] S. Aly et al. Jig-shape static aeroelastic wing design problem: A decoupled approach. *Journal Aircraft*, 39:1061–1066, 2002.

[32] Ansys. Introduction to ansys mechanical apdl, Accessed on 14 april 2021.

[33] ANSYS Inc. Ansys mechanical apdl element reference, 2011.

[34] F. Afonso et al. The effect of stiffness and geometric parameters on the nonlinear aeroelastic performance of high aspect ratio wings. *Proceedings of the Institution of Mechanical Engineers, Part G: Journal of Aerospace Engineering*, 231(10):1824–1850, 2017.